Atmos. Meas. Tech., 15, 1–13, 2022
https://doi.org/10.5194/amt-15-1-2022
© Author(s) 2022. This work is distributed under
the Creative Commons Attribution 4.0 License.

Atmospheric Measurement Techniques
Open Access

Identification, monitoring, and reaction kinetics of reactive trace species using time-resolved mid-infrared quantum cascade laser absorption spectroscopy: development, characterisation, and initial results for the CH_2OO Criegee intermediate

Zara S. Mir[1], Matthew Jamieson[1], Nicholas R. Greenall[1], Paul W. Seakins[1], Mark A. Blitz[1,2], and Daniel Stone[1]

[1]School of Chemistry, University of Leeds, Leeds, LS2 9JT, UK
[2]National Centre for Atmospheric Science, University of Leeds, Leeds, LS2 9JT, UK

Correspondence: Daniel Stone (d.stone@leeds.ac.uk)

Received: 13 December 2021 – Discussion started: 7 February 2022
Revised: 17 March 2022 – Accepted: 27 March 2022 – Published:

Abstract. The chemistry and reaction kinetics of reactive species dominate changes to the composition of complex chemical systems, including Earth's atmosphere. Laboratory experiments to identify reactive species and their reaction products and to monitor their reaction kinetics and product yields are key to our understanding of complex systems. In this work we describe the development and characterisation of an experiment using laser flash photolysis coupled with time-resolved mid-infrared (mid-IR) quantum cascade laser (QCL) absorption spectroscopy, with initial results reported for measurements of the infrared spectrum, kinetics, and product yields for the reaction of the CH_2OO Criegee intermediate with SO_2. The instrument presented has high spectral ($< 0.004\,cm^{-1}$) and temporal ($< 5\,\mu s$) resolution and is able to monitor kinetics with a dynamic range to at least $20\,000\,s^{-1}$. Results obtained at 298 K and pressures between 20 and 100 Torr gave a rate coefficient for the reaction of CH_2OO with SO_2 of $(3.83 \pm 0.63) \times 10^{-11}\,cm^3\,s^{-1}$, which compares well to the current IUPAC recommendation of $\left(3.70^{+0.45}_{-0.40}\right) \times 10^{-11}\,cm^3\,s^{-1}$. A limit of detection of 4.0×10^{-5}, in absorbance terms, can be achieved, which equates to a limit of detection of $\sim 2 \times 10^{11}\,cm^{-3}$ for CH_2OO, monitored at $1285.7\,cm^{-1}$, based on the detection path length of (218 ± 20) cm. Initial results, directly monitoring SO_3 at $1388.7\,cm^{-1}$, demonstrate that SO_3 is the reaction product for $CH_2OO + SO_2$. The use of mid-IR QCL absorption spectroscopy offers significant advantages over alternative techniques commonly used to determine reaction kinetics, such as laser-induced fluorescence (LIF) or ultraviolet absorption spectroscopy, owing to the greater number of species to which IR measurements can be applied. There are also significant advantages over alternative IR techniques, such as step-scan FT-IR, owing to the coherence and increased intensity and spectral resolution of the QCL source and in terms of cost. The instrument described in this work has potential applications in atmospheric chemistry, astrochemistry, combustion chemistry, and in the monitoring of trace species in industrial processes and medical diagnostics.

1 Introduction

The behaviour of reactive intermediates is critical to understanding the chemistry of complex systems. In the gas phase, reactive intermediates govern the chemistry and composition of planetary atmospheres (Blitz and Seakins, 2012) and the interstellar medium and star-forming regions (Herbst, 2001) as well as control combustion processes and autoignition (Pilling et al., 1995; Zador et al., 2011). In the Earth's atmosphere, the chemistry of reactive intermediates determines the rate at which compounds emitted into the atmosphere are removed and transformed into other species and thus drives changes to air quality and climate (Monks, 2005; Von Schneidemesser et al., 2015).

Experimental investigation of the spectroscopy, kinetics, and reaction mechanisms of reactive intermediates is key

to understanding the behaviour of such species, requiring sensitive and specific detection techniques capable of monitoring changes in concentrations during the course of reactions commonly occurring on microsecond to millisecond timescales. Flash photolysis experiments, in which a reactive species is generated rapidly by a brief pulse of light from a flashlamp or, more commonly, a laser and then monitored throughout its subsequent reactions, have enabled the study of many reactions of interest. However, while the flash photolysis method can be coupled to a wide range of techniques to determine the kinetics of a reaction, limitations remain, particularly surrounding the identification of reaction products and measurements of product yields (Seakins, 2007).

For the study of fast reactions, spectroscopic or mass-spectrometric techniques are typically required to provide the necessary time resolution. Laser-induced fluorescence (LIF) spectroscopy has been demonstrated to have both high sensitivity and specificity for the measurement and identification of reactants and products but is not an absolute technique and so requires either calibration or the use of an internal standard to determine yields (Carr et al., 2007). Moreover, LIF can only be applied to the relatively small number of species that exhibit fluorescence spectra. Mass spectrometry can be applied more widely, particularly if soft-ionisation techniques such as photoionisation are employed, but such techniques can be costly and require sampling of a reaction mixture into an ionisation and detection region, which can limit investigations to low-pressure regimes (Fockenberg et al., 1999; Blitz et al., 2007; Osborn et al., 2008; Middaugh et al., 2018). Absorption techniques can therefore be beneficial as these can provide absolute measurements over a wide range of temperatures and pressures.

Absorption measurements based on ultraviolet (UV) spectroscopy have been used successfully to measure the kinetics of a broad variety of reactions, with advantages for radical–radical reactions where absolute concentrations are required. While UV absorption spectra can be relatively broad and featureless (Orlando and Tyndall, 2012), developments in the use of broadband light sources have enabled the separation of multiple absorbing species with overlapping spectra (Cossel et al., 2017), particularly if any of the spectra display a distinctive vibronic structure. Multipass (Lewis et al., 2018) and cavity-enhanced techniques (Cossel et al., 2017) can also offer significant improvements to sensitivity. However, UV absorption experiments are typically employed to monitor changes in reactant concentrations to determine reaction kinetics, but identification of products and measurement of product yields are often not possible owing to a lack of suitable UV absorption features or CE1 low-UV-absorption cross-sections for product species. There is thus interest in the development and use of infrared (IR) techniques which, despite lower-absorption cross-sections compared to the UV, have the potential to be implemented more extensively since most species exhibit some features in the IR region of the spectrum, with IR spectroscopy offering the potential for structural determination and unique identification of reactants and products. Infrared absorption techniques are also often advantageous over other spectroscopic methods, particularly at relatively low temperatures and pressures, since IR transitions are typically not dissociative (Taatjes and Hershberger, 2001; Hodgkinson and Tatam, 2013) and as a result do not suffer lifetime broadening or probe-induced photochemistry. Additionally, Doppler broadening in the IR is less problematic than in the UV or visible, leading to better resolution of closely spaced features (Taatjes and Hershberger, 2001; Hodgkinson and Tatam, 2013).

For many reactions of atmospheric interest, products have been determined by long-path Fourier transform infrared (FT-IR) absorption spectroscopy in atmospheric simulation chambers used to study reactions at a mechanistic level (Doussin et al., 1997; Glowacki et al., 2007; Nilsson et al., 2009; Seakins, 2010), but this method has relatively poor time resolution compared to direct studies of elementary reactions. Such studies can be influenced by secondary chemistry and wall reactions, which may transform reactive products into more stable species on the timescale of the experiment. Step-scan FT-IR experiments (Su et al., 2013; Huang et al., 2007), in which spectra are recorded at successive time points during the course of a reaction, offer improved time resolution and aid direct identification of reaction products. However, step-scan FT-IR has relatively poor sensitivity and spectral resolution compared to other techniques and is not typically employed to investigate reaction kinetics owing to the length of time required to record a suitable time profile.

Diode lasers (Taatjes and Hershberger, 2001), quantum cascade lasers (QCLs) (Faist et al., 1994; Hofstetter and Faist, 2003; Yao et al., 2012; Zhang et al., 2014; Pecharroman-Gallego, 2013), and frequency comb lasers (Fleisher et al., 2014; Bjork et al., 2016; Roberts et al., 2020) can be used to give both high spectral resolution and high temporal resolution and can be applied to measurements of transient species. Frequency comb lasers can provide extremely high-resolution spectra, but there are, at present, relatively few examples (Bjork et al., 2016) of their application in chemistry and chemical kinetics owing to relatively high cost and complexity of the experimental set-up. In contrast to mid-IR lead salt diode lasers, mid-infrared QCLs do not require cryogenic operation and do not suffer issues related to mode-hopping, uneven diode quality, or unpredictable tunability (Hodgkinson and Tatam, 2013). The spectral output of QCLs can be tailored to transitions over a wide range, providing access to regions of the spectrum not readily accessible with diode lasers or frequency comb lasers (Shahmohammadi et al., 2019; Yao et al., 2012; Zhang et al., 2014). QCLs have high output powers and can reach several hundred milliwatts to ~ 1 W (Hodgkinson and Tatam, 2013; Pecharroman-Gallego, 2013; Yao et al., 2012; Zhang et al., 2014), compared to typical powers of a few milliwatts for diode lasers (Hodgkinson and Tatam, 2013), and absorbances on the order of 10^{-6} have been reported for QCL-based infrared absorp-

Please note the remarks at the end of the manuscript.

tion experiments for stable species (Borri et al., 2006). The high resolution, specificity, and sensitivity of QCL-based absorption techniques have led to the development of a number of field instruments for detection of trace species in the atmosphere (Li et al., 2013; Du et al., 2019), including CH_4 (McManus et al., 2010; Kostinek et al., 2019), CO_2 (Kostinek et al., 2019), OCS (Mcmanus et al., 2010), N_2O (Mcmanus et al., 2010; Banik et al., 2017; Kostinek et al., 2019), H_2O (Mcmanus et al., 2010), HCOOH (Herndon et al., 2007), and HONO (Cui et al., 2019), which can be challenging to monitor by other methods. The high power and spectral resolution of QCL light sources, enabling sensitive and specific experiments in regions of the spectrum characterised by strong fundamental transitions, have also led to interest from the chemical kinetics community.

QCLs consist of layers of semiconductor material that create a series of coupled quantum wells in which the layer thickness determines the depth of the quantum well and thus the energy of emitted photons (Yao et al., 2012; Faist et al., 1994). In contrast to diode lasers, which involve electronic transitions between conduction and valence bands, laser action in QCLs involves intersub-band transitions within the conduction band, typically via a three-level system (Yao et al., 2012; Gmachl et al., 2001; Curl et al., 2010). In the absence of an electric field, electrons are confined in the quantum wells within an injector region. When an electric field is applied, the quantum wells within the injector region align, and electrons are injected into an upper intersub-band state, creating a population inversion with an intermediate level. Relaxation of electrons to a lower intersub-band state, resulting in photon emission, followed by rapid tunnelling of electrons from the lower intersub-band state into the injector region of the next layer creates a cascade of electrons as the layer structure is traversed, leading to increased photon emission and significant optical gain (Yao et al., 2012). Broadband emission can be achieved using external cavity (EC) QCLs, which can give coverage of several hundred wavenumbers, or Fabry–Perót (FP) QCLs, giving coverage of $\sim 50\,cm^{-1}$, while single-mode emission relevant to this work is achieved using distributed feedback (DFB) QCLs (Shahmohammadi et al., 2019). For emission in the mid-IR, DFB QCLs can be operated at room temperature, with control of the temperature of the semiconductor and the applied current allowing fine-tuning of the laser output within a range of $\sim 5\,cm^{-1}$ (Shahmohammadi et al., 2019).

Pulsed QCLs have been used to measure the production of CO in the combustion of *n*-heptane (Nasir and Farooq, 2019) and have been used to determine the IR absorption spectrum and cross-sections of the Criegee intermediate CH_2OO (Chang et al., 2017, 2018b; Luo et al., 2018a). CH_2OO is a reactive species produced in the atmosphere during the ozonolysis of unsaturated volatile organic compounds (VOCs) that has been of recent interest as a result of developments in photolytic sources (Welz et al., 2012) for detailed laboratory studies which have revealed a more significant role in atmospheric chemistry than previously expected (Chhantyal-Pun et al., 2020; Percival et al., 2013). Quasi-continuous QCLs, pulsed QCLs in which the pulse period is relatively long compared to the lifetime of the species under investigation, have also been used to investigate the spectra and kinetics of CH_2OO (Chang et al., 2018a), and continuous-wave (cw) QCLs have been used to investigate the kinetics of CH_2OO (Luo et al., 2018b, 2019; Li et al., 2019, 2020) and other larger Criegee intermediates (Luo et al., 2018b) as well as the spectroscopy and kinetics of the atmospherically important peroxy radicals HO_2 (Miyano and Tonokura, 2011; Sakamoto and Tonokura, 2012) and CH_3O_2 (Chattopadhyay et al., 2018). While mid-IR QCLs have been employed to study the kinetics and spectroscopy of reactive species relevant to atmospheric chemistry, there are still few examples of the use of QCL-based techniques to identify reaction products and to determine product yields.

In this work, we report the development, characterisation, and initial results from a robust and economical experiment using laser flash photolysis coupled with time-resolved mid-infrared QCL absorption spectroscopy that can be applied to a wide range of problems in atmospheric chemistry and beyond. We describe the experimental set-up (Sect. 2), time-averaged measurements of absorption spectra of stable species (Sect. 3), and time-resolved measurements of photolytically generated species and reaction products (Sect. 4) that can be used to determine spectra of reactive species as well as reaction kinetics and product yields. Factors affecting the limit of detection are also discussed (Sect. 5).

2 Experimental

A schematic of the experimental set-up is given in Fig. 1. The reaction cell has been used previously in IR diode laser experiments (Qian et al., 2000, 2001; Choi et al., 2006) and consisted of a central cylindrical stainless steel cell 70 cm in length and with an internal diameter of 40 mm, connected via bellows at each end to stainless steel sections 15 cm in length and with an internal diameter of 7 cm, which are furnished with 60 mm diameter UV grade CaF_2 windows (Crystran).

Reagent gases, such as NO (BOC special gases, 99.5 %) and SO_2 (Sigma-Aldrich, 99.9 %) (Sect. 4), were prepared manometrically at known concentrations in N_2 and stored in glass bulbs before mixing with N_2 (BOC, 99.99 %), and in some cases O_2 (BOC, 99.999 %), in a stainless steel mixing line at known flow rates determined by calibrated mass flow controllers (Tylan, 2900 series). For experiments involving species in the liquid phase at room temperature, such as CH_3I (Sigma-Aldrich, 99 %) and CH_2I_2 (Sigma-Aldrich, 99 %) (Sects. 3 and 4), the liquid was contained within a bubbler held at 0 °C and entrained into the vapour phase by passing a known flow of N_2 through the bubbler, which was subsequently combined with the main gas flow in the mixing line. Gas mixtures prepared in the mixing line were

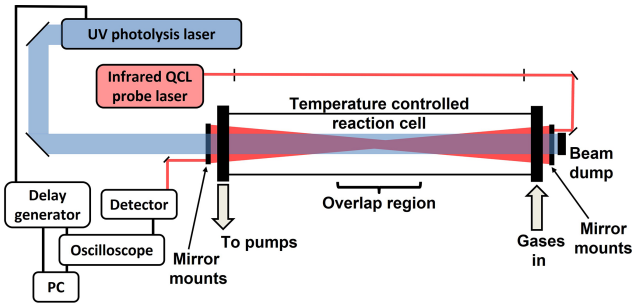

Figure 1. Schematic of the experimental apparatus. The probe beam passes through the reaction cell multiple times, with mirrors in a circular arrangement on the mounts positioned at each end of the cell such that the probe passes from the top of the cell to the bottom or from left to right in any individual pass through the cell, resulting in the overlap between the photolysis and probe beams occurring in the centre of the cell.

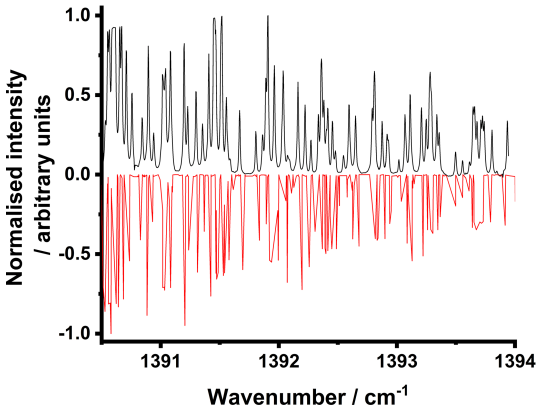

Figure 2. Normalised observed spectrum (black) for SO_2 with the corresponding normalised spectrum reported on the HITRAN database (Gordon et al., 2017; Kochanov et al., 2019) (multiplied by -1) (red). HITRAN data are given as line intensities and thus do not account for any line broadening.

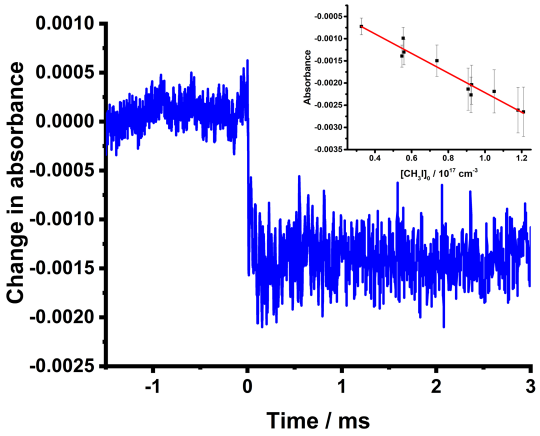

Figure 3. Changes in absorbance at $\sim 1287\,\mathrm{cm}^{-1}$ observed on 266 nm photolysis of CH_3I. For the data shown in the main figure, $[CH_3I]_0 = 5.5 \times 10^{16}\,\mathrm{cm}^{-3}$, $p = 50$ Torr, and laser fluence is $30\,\mathrm{mJ\,cm}^{-2}$. The data shown are the means of 200 photolysis shots. The inset shows the average post-photolysis ($0.5\,\mathrm{ms} < t < 3$ ms) change in absorbance as a function of the initial CH_3I concentration (black points) with the line of best fit (red). The pre-photolysis region for these experiments was defined as $-1.5\,\mathrm{ms} < t < -0.5\,\mathrm{ms}$.

passed into the reaction cell via one of the end sections, with the other end section connected to a rotary pump (Edwards E2M28). The total pressure in the cell was monitored by a capacitance manometer (MKS Instruments, 626A) and controlled by throttling the exit of the cell to the pump, with cell pressures from < 5 Torr to above atmospheric pressure achievable. Experiments reported in this work were performed at room temperature, although temperature control of the reaction cell is possible by surrounding the cell with ceramic heaters (Watlow, WATROD tubular heater), a bath filled with an appropriate solvent (e.g. methanol) chilled by a refrigerated immersion probe (LabPlant refrigerated immersion probe, RP-100CD), or a dry ice slush bath (Choi et al., 2006), all of which are available in this laboratory.

For experiments involving reactive species generated by photolysis, chemistry within the cell was initiated by the fourth harmonic of an Nd:YAG laser (Continuum Powerlite 8010), giving 266 nm (typical fluence $30\,\mathrm{mJ\,cm}^{-2}$). The photolysis beam has diameter ~ 1 cm and was aligned through the centre of the reaction cell using a pair of mirrors (Thorlabs NB1-K04). For all experiments reported in this work, the repetition rate of the photolysis laser was set to 1 Hz, and the flow rate through the reaction cell was sufficiently high to ensure that a fresh gas mixture was photolysed for each photolysis shot.

Infrared probe radiation was provided by one of two cw mid-IR DFB QCLs, depending on the application, providing radiation at wavenumbers of $\sim 1286\,\mathrm{cm}^{-1}$ ($\sim 7.77\,\mu$m) (Alpes Lasers) and $\sim 1390\,\mathrm{cm}^{-1}$ ($\sim 7.19\,\mu$m) (Thorlabs) with a tuning range of $\sim 5\,\mathrm{cm}^{-1}$ around each centre. Temperature and current control of the QCL, which determines the precise output wavenumber of a given QCL, were controlled by a combined laser current and thermoelectric (TEC) controller (Thorlabs, ITC4002QCL). The current and TEC controller was operated in constant-current mode, which provides current control up to 2 A in 0.1 mA steps with accuracy $\pm(0.1\,\% + 800\,\mu\mathrm{A})$ and stability $< 150\,\mu$A, and temperature control between 123 and 423 K in 0.001 K steps with stability < 0.002 K.

QCLs were housed in high heat load (HHL) packages, which were each integrated with a ZnSe aspheric lens to collimate the output beam (divergence < 6 mrad) and mounted on a heat sink (Hamamatsu HHL mount, A117909-1) to dissipate excess heat. Mounted QCLs were positioned on a pitch-and-yaw stage (Thorlabs, PY003/M) on an adjustable-height platform (Thorlabs, C1519/M) to aid alignment through two adjustable aperture irises (Thorlabs, ID8/M) which were separated by > 70 cm. A collimated

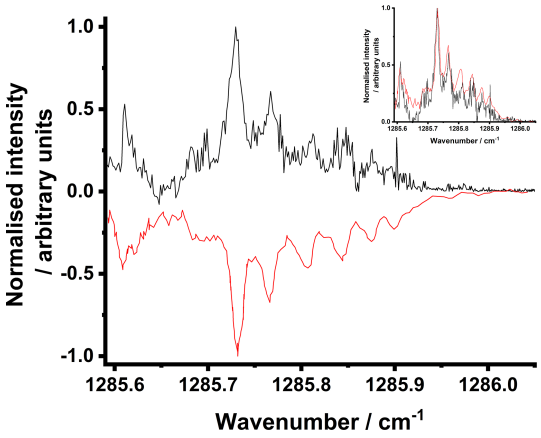

Figure 4. Normalised CH_2OO spectrum obtained in this work (black) and that reported previously (Chang et al., 2018a) (multiplied by −1) (red). Measurements made in this work were obtained at a total pressure of 50 Torr at 298 K in the absence of SO_2, with $[CH_2I_2] \sim 2 \times 10^{14}\,cm^{-3}$ and a laser fluence of $30\,mJ\,cm^{-2}$. The data shown are the means of 1000 photolysis shots at each current setting on the QCL with the wavenumber calibrated using the results reported in previous work (Chang et al., 2018a). The inset plot shows the normalised spectra obtained in this work (black) and by Chang et al. (2018a) (red) on the same scale. The experiments and the HITRAN database indicate that there is no appreciable absorption by CH_2I_2 in this region of the spectrum.

laser diode operating at 635 nm (Thorlabs, CPS635R) was co-aligned through the irises via a mirror (Thorlabs, PF10-03-G01) on a flip mount (Thorlabs, FM90/M) to guide alignment of the QCL beam through the reaction cell. A pair of 1″ Al mirrors (Thorlabs, PF10-03-G01), situated after the second iris, were used to direct the beam into the reaction cell, with the beam focussed into the centre of the cell by a 1″ ZnSe plano-convex lens (focal length 1000 mm, Thorlabs, LA7753-G).

The probe IR beam was aligned through the cell in a multipass arrangement to increase the total path length and sensitivity, with the mirrors reflecting the probe beam external to the cell. Custom-built mirror mounts with a central 12 mm hole were located exterior to the cell and were used to mount six Ag mirrors (12 mm diameter, 2.4 m radius of curvature, Knight Optical) in a circular arrangement at each end of the cell, similarly to the arrangement previously described for the multipass UV absorption experiment in this laboratory (Lewis et al., 2018). These mirrors can be aligned independently of each other via three alignment screws for each mirror and enable up to 13 passes through the reaction cell. On the final pass of the IR probe beam through the cell the beam was directed onto a 1″ Au off-axis parabolic mirror (reflected focal length 4″, Thorlabs, MPD149-M01) and focussed onto the detector. The detector was a DC-coupled photovoltaic mercury–cadmium–telluride (MCT) detector (Vigo System, PVMI-3TE-8-2x2-TO8-wBaF2-35), integrated with a preamplifier (Vigo System, MIP-DC-100k-F-M4) with bandwidth up to 100 kHz.

The signal was transferred to an oscilloscope via a sheathed BNC cable for data collection and processing, with the settings on the oscilloscope dictating the time resolution of the experiment. For measurements of stable species, all spectra reported in this work were recorded using a traditional oscilloscope (LeCroy WaveRunner-2, LT262, 350 MHz, $1\,GS\,s^{-1}$ sample rate, 8 bit resolution), while for reactive species produced in photolytic experiments, the use of a PicoScope (Pico Technology, PicoScope 6402C, 250 MHz, $5\,GS\,s^{-1}$ sample rate, 12 bit resolution) was also investigated. Data acquisition is discussed further in Sects. 4 and 5.

Synchronisation of the photolysis laser and oscilloscope was achieved using a custom-built digital delay generator based on National Instruments hardware, with the overall experiment and data collection controlled by custom LabVIEW software. In addition to measurements of the probe intensity as a function of time at a fixed QCL output wavenumber, the software enabled stepping of the current applied to the QCL at a set temperature to vary the output wavenumber, which is used to measure the variation in the probe intensity across the tuning range with and without a sample present to determine the spectra of stable species. For reactive species produced by, or following, photolysis, the average pre- and post-photolysis intensities were determined over specified time ranges at each current setting to give the absorption spectrum. Further details are given in Sect. 4.

3 Time-averaged experiments

Characterisation of the output wavenumber of the QCL was achieved through measurement of the absorption spectra of stable species with well-defined rovibrational spectra. Spectra for SO_2 and CH_3I were recorded by measuring the variation in QCL intensity across the tuning range of the QCL for the cell filled with N_2 and for the cell filled with a mixture of N_2 and the species of interest under otherwise identical conditions. The absorbance $A_{\tilde{\nu}}$ at each wavenumber $\tilde{\nu}$ was calculated from the Beer–Lambert law (Eq. 1):

$$A_{\tilde{\nu}} = \ln\left(\frac{I_{\tilde{\nu},0}}{I_{\tilde{\nu}}}\right) = \sigma_{\tilde{\nu}}[C]l, \quad (1)$$

where $I_{\tilde{\nu},0}$ and $I_{\tilde{\nu}}$ are the intensities at wavenumber $\tilde{\nu}$ without and with the species of interest present, respectively; $\sigma_{\tilde{\nu}}$ is the absorption cross-section at wavenumber $\tilde{\nu}$; $[C]$ is the concentration; and l is the path length of the IR probe beam through the sample. In measurements of stable species in experiments in which no photolysis takes place, the total path length can be determined from the geometry of the cell and optical arrangement and was ~ 13 m for the measurements discussed here.

Figure 2 shows the normalised observed absorbance spectrum for SO_2 alongside the comparison to the normalised spectrum available on the HITRAN database (Gordon et al., 2017; Kochanov et al., 2019) to illustrate the calibration of the QCL output wavenumber with the current. The measured spectrum indicates the capacity for high-resolution measurements made possible by the narrow laser linewidth.

4 Time-resolved experiments

4.1 Stable species

Photolytic experiments were initially performed for a system demonstrating a step change in the time-resolved signal intensity at a given wavenumber on photolysis, such that photolysis led to the removal of the species under investigation with no significant further chemistry on the timescale of the measurements. Figure 3 shows the time-resolved absorbance observed on 266 nm photolysis of CH_3I–N_2 mixtures and the average post-photolysis change in absorbance as a function of the initial CH_3I concentration. Photolysis of CH_3I leads to a decrease in concentration and thus an increase in signal intensity and a negative absorbance. The extent of change in absorbance reflects the absorption cross-section at the measurement wavenumber, the change in concentration, and the effective path length resulting from the overlap between the UV photolysis beam and the IR probe beam. For the 266 nm laser fluence of 30 mJ cm^{-2} and CH_3I absorption cross-section of 9.7×10^{-19} cm^2 at the photolysis wavelength (IUPAC) (Atkinson et al., 2008), a change in CH_3I concentration of 4 % is expected on photolysis. For the absorbance data shown in Fig. 3 and an estimated infrared cross-section of CH_3I at ~ 1287 cm^{-1} of 2×10^{-21} cm^2 (HITRAN) (Gordon et al., 2017; Kochanov et al., 2019), the effective path length of the IR probe beam for these measurements can thus be estimated as (290 ± 30) cm. The effective path length is discussed further in Sect. 4.2.

4.2 Reactive species

The behaviour of reactive species was investigated through 266 nm photolysis of CH_2I_2–O_2–N_2 and CH_2I_2–O_2–N_2–SO_2 mixtures (Welz et al., 2012), resulting in the rapid production ($k_{CH2I+O2}[O_2] > 2 \times 10^5$ s^{-1}) of the Criegee intermediate CH_2OO (Reactions R1–R2), followed by its removal through the CH_2OO self-reaction (Reaction R3), $CH_2OO + I$ (Reaction R4), $CH_2OO + SO_2$ (Reaction R5), and physical losses such as diffusion (Reaction R6):

$$CH_2I_2 + h\nu \rightarrow CH_2I + I \quad \text{(R1)}$$

$$CH_2I + O_2 \rightarrow CH_2OO + I \quad \text{(R2a)}$$

$$\rightarrow CH_2IO_2 \quad \text{(R2b)}$$

$$CH_2OO + CH_2OO \rightarrow 2HCHO + O_2 \quad \text{(R3)}$$

$$CH_2OO + I \rightarrow CH_2IO_2 \quad \text{(R4)}$$

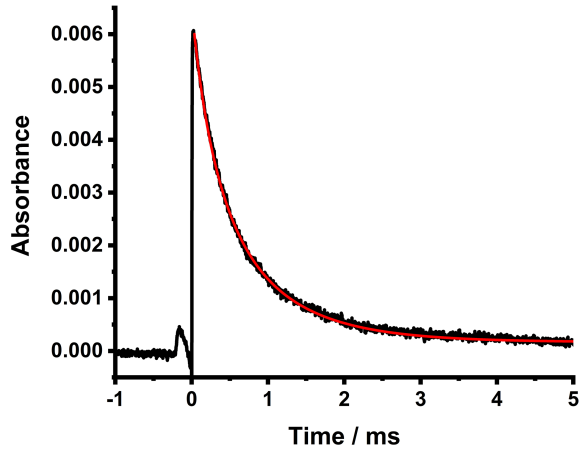

Figure 5. Time-resolved absorbance for CH_2OO obtained at a wavenumber of ~ 1285.73 cm^{-1}. Data are the average of 1000 photolysis shots at a total pressure of 50 Torr. For these data, $[CH_2I_2] = 1.6 \times 10^{14}$ cm^{-3}, and $[SO_2] = 0$. The fit to the data using the model containing the reactions given in Table 1 is shown by the solid red line, which gave $k_{phys} = (504 \pm 40)$ s^{-1} and $l = (218 \pm 20)$ cm.

$$CH_2OO + SO_2 \rightarrow HCHO + SO_3 \quad \text{(R5)}$$

$$CH_2OO \rightarrow \text{diffusion.} \quad \text{(R6)}$$

TS2 Figure 4 shows the spectrum obtained in the absence of SO_2 by measuring the average pre- and post-photolysis absorbances for an observed time profile for a given QCL current setting, and thus a given wavenumber, and then stepping to the next current setting and repeating. The step in current for these experiments was 0.1 mA, the smallest step size available with the current controller used, giving steps of < 0.002 cm^{-1} across the range investigated. The pre-photolysis region was defined as -4000 to 500 µs, owing to detection of some radiofrequency noise associated with the Q-switch delay of the photolysis laser, which was set to 280 µs (i.e. the Q-switch fires at $t = -280$ µs), and the post-photolysis region as 500 to 6000 µs, where $t = 0$ is the time at which the photolysis laser is fired. Experiments were performed at 50 Torr, and each time-resolved trace was averaged for 1000 photolysis shots. The concentration of CH_2I_2 for these experiments, determined from the flow rates of gases in the cell, the vapour pressure of CH_2I_2, and measurements of the saturation of the flow with CH_2I_2 in previous experiments with similar flow rates, was $\sim 2 \times 10^{14}$ cm^{-3}, and the 266 nm laser fluence was 30 mJ cm^{-2}, giving an expected initial CH_2OO concentration of $\sim 7 \times 10^{12}$ cm^{-3} using previous measurements of the yield of Reaction (R2a) (Stone et al., 2013). The spectrum measured in this work is in good agreement with that reported previously (Chang et al., 2017, 2018a). The resolution observed in this work is similar to the resolution of < 0.004 cm^{-1} reported in previous work (Chang et al., 2017) based on the observation of non-overlapped peaks, although the linewidth of the QCLs

Please note the remarks at the end of the manuscript.

Table 1. Reactions and rate coefficients used in the model to fit to experimental observations of CH_2OO absorbances to determine the effective path length of the probe beam. The absorbances at time zero, k_{phys} (describing physical losses of CH_2OO such as diffusion), and the effective path length were fit in the model. Initial concentrations of CH_2I, iodine atoms, and CH_2IO_2 were determined relative to the initial concentrations determined for CH_2OO using the results of our previous measurements of the yields of $CH_2I + O_2$, where β indicates the yield of CH_2OO from $CH_2I + O_2$ (Stone et al., 2013). The rate coefficient k_{phys} represents physical losses of CH_2OO such as diffusion out of the probe region and was determined in the fits to this work.

Reaction number	Reaction	Rate coefficient, $k^a/cm^3\,s^{-1}$ or k^b/s^{-1}	Reference
(R2a)	$CH_2I + O_2 \rightarrow CH_2OO + I$	$\beta \times 1.5 \times 10^{-12}$	Stone et al. (2013), Masaki et al. (1995), Eskola et al. (2006)
(R2b)	$CH_2I + O_2 \rightarrow CH_2IO_2$ TS1	$(1\text{-}\beta) \times 1.5 \times 10^{-12}$	Stone et al. (2013), Masaki et al. (1995), Eskola et al. (2006)
(R3)	$CH_2OO + CH_2OO \rightarrow 2\,HCHO + O_2$	8.0×10^{-11}	Mir et al. (2020)
(R4)	$CH_2OO + I \rightarrow$ products	3.4×10^{-11}	Mir et al. (2020)
(R6)	$CH_2OO \rightarrow$ loss	k_{phys}	Determined in fit
(R7)	$CH_2IO_2 + CH_2IO_2 \rightarrow 2\,CH_2IO + O_2$	9.0×10^{-11}	Gravestock et al. (2010)
(R8)	$CH_2IO_2 + I \rightarrow CH_2IO + IO$	3.5×10^{-11}	Gravestock et al. (2010)
(R9)	$CH_2IO \rightarrow HCHO + I$	1×10^5	Gravestock et al. (2010)

[a] Second-order reactions. [b] First-order reactions.

used in this work and in that in the previous measurement of the spectrum (Chang et al., 2018a) should enable higher resolution of $< 0.002\,cm^{-1}$ when observing species with more closely spaced features.

Kinetics describing the loss of CH_2OO were monitored in separate experiments with the QCL set at the peak in the CH_2OO spectrum ($\sim 1285.73\,cm^{-1}$). Figure 5 shows an example CH_2OO decay obtained at a pressure of 50 Torr in the absence of SO_2. The QCL can be tuned to a particular spectral feature and remain tuned to that feature for prolonged periods of time during which kinetics experiments and repeat measurements can be performed without any drift in spectral position. QCLs thus offer significant advantages for kinetics experiments over alternative mid-IR sources such as lead salt diode lasers, which can suffer from mode-hopping, uneven diode quality, and unpredictable tunability (Hodgkinson and Tatam, 2013). Such behaviour of alternative mid-IR sources can require sophisticated techniques to scan over a spectral feature, identify the peak, and then wait until the laser remains stable for a sufficient period of time to perform the desired experiment (Qian et al., 2000).

In the absence of any additional co-reactant such as SO_2, the loss of CH_2OO (as shown in Fig. 5) is dominated by Reactions (R3) and (R4) (Mir et al., 2020). Since Reactions (R3) and (R4) are not first-order, the kinetics describing the loss of CH_2OO are dependent on absolute CH_2OO concentrations. The kinetics of Reactions (R3) and (R4) have been determined in our previous work (Mir et al., 2020), and the absorption cross-section of CH_2OO has been measured (Chang et al., 2018b) to be $(3.9 \pm 0.6) \times 10^{-18}\,cm^2$ at the peak of its spectrum at $\sim 1285.73\,cm^{-1}$ at a total pressure of 50 Torr. The numerical integration package FACSIMILE (MCPA Software, 2014) was therefore used to fit to the measured absorbances to determine the physical losses of CH_2OO owing to diffusion out of the probe beam (approximated by a first-order rate coefficient k_{phys}) and the effective path length (l) of the probe beam required to convert the absorbances to concentrations compatible with the measured CH_2OO absorption cross-section of $(3.9 \pm 0.6) \times 10^{-18}\,cm^2$ (Chang et al., 2018b) and the known kinetics for the mechanism used in the model (Table 1). Fits were performed for experiments in which precursor concentrations were varied in the range $0.1\text{–}5.0 \times 10^{14}\,cm^{-3}$. Initial concentrations of CH_2I, iodine atoms, and CH_2IO_2 were calculated in the model relative to those for CH_2OO using the yields of Reactions (R1) and (R2) determined in our previous work (Stone et al., 2013).

The fits to the measured absorbances gave $k_{phys} = (504 \pm 40)\,s^{-1}$ and an effective path length of (218 ± 20) cm. Figure 5 shows an example fit to the data. While the effective path length determined from experiments involving CH_2OO ((218 ± 20) cm) is lower than that determined from experiments involving CH_3I (290 ± 30) cm; Sect. 4.1), the results are in broad agreement, and the system was realigned between experiments, which may explain the difference.

In the presence of excess SO_2 the observed decays of CH_2OO are dominated by Reaction (R5), and the loss of CH_2OO can be described by pseudo-first-order kinetics

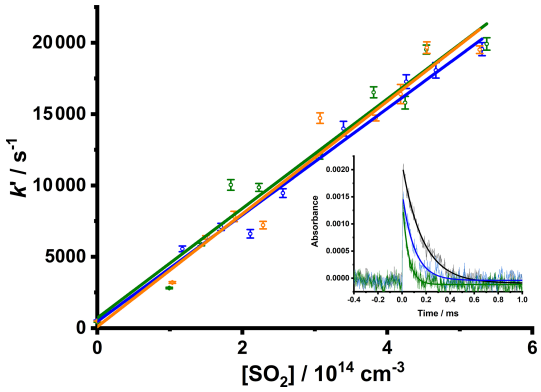

Figure 6. Bimolecular plots of the pseudo-first-order rate coefficients, k', determined from fits of Eq. (2), to observed CH_2OO decays as a function of $[SO_2]$ at total pressures of 20 Torr (blue points and line; giving k_5 $(3.73 \pm 0.19) \times 10^{-11}$ $cm^3\,s^{-1}$, intercept $= (500 \pm 600\,s^{-1})$), 50 Torr (green points and line; giving $k_5 = (3.84 \pm 0.27) \times 10^{-11}$ $cm^3\,s^{-1}$, intercept $= (700 \pm 900\,s^{-1})$), and 100 Torr (orange points and line; giving $k_5 = (3.95 \pm 0.28) \times 10^{-11}$ $cm^3\,s^{-1}$, intercept $= (100 \pm 900\,s^{-1})$). The data compare well to the current IUPAC recommendation of $\left(3.70^{+0.45}_{-0.40}\right) \times 10^{-11}\,cm^3\,s^{-1}$ (Cox et al., 2020). For these data $T = 298$ K, and initial CH_2I_2 concentrations were in the range 2.1–$9.5 \times 10^{14}\,cm^{-3}$. Error bars are 1σ from the fits to Eq. (2). The inset plot shows typical plots obtained for 250 photolysis shots at $p = 50$ Torr with the fits to Eq. (2) (for the data shown in black, $[SO_2] = 1.4 \times 10^{14}\,cm^{-3}$, and $k' = (5860 \pm 90)\,s^{-1}$; for the data shown in blue, $[SO_2] = 2.2 \times 10^{14}\,cm^{-3}$, and $k' = (9860 \pm 280)\,s^{-1}$; and for the data shown in green, $[SO_2] = 5.4 \times 10^{14}\,cm^{-3}$, and $k' = (19\,920 \pm 440)\,s^{-1}$).

(Eq. 2).

$$A_t = A_{t=0} \exp(-k't), \tag{2}$$

TS3 where A_t is the absorbance at time t; A_0 is the absorbance at time zero; and k' is the pseudo-first-order rate coefficient, given by $k' = k_5\,[SO_2] + k_{phys}$, where k_5 is the bimolecular rate coefficient for reaction between CH_2OO and SO_2, and k_{phys} is the rate coefficient representing physical losses of CH_2OO such as diffusion out of the probe region.

Fits of Eq. (2) to the observed CH_2OO decays obtained in the presence of SO_2 were performed to determine the pseudo-first-order rate coefficients, k', which can be plotted against the known SO_2 concentration (Sect. 2) to give the bimolecular rate coefficient k_5. Figure 6 shows typical bimolecular plots of k' against the SO_2 concentration, giving $k_5 = (3.73 \pm 0.19) \times 10^{-11}\,cm^3\,s^{-1}$ at 20 Torr, $k_5 = (3.84 \pm 0.27) \times 10^{-11}\,cm^3\,s^{-1}$ at 50 Torr, and $k_5 = (3.95 \pm 0.28) \times 10^{-11}\,cm^3\,s^{-1}$ at 100 Torr, in good agreement with the current IUPAC-recommended value of $\left(3.70^{+0.45}_{-0.40}\right) \times 10^{-11}\,cm^3\,s^{-1}$ (Cox et al., 2020). The data shown in Fig. 6 indicate that the experiment developed in this work is able to measure the spectra and kinetics of reactive species to a high degree of accuracy and precision and that a high dynamic range up to at least $20\,000\,s^{-1}$ can be achieved.

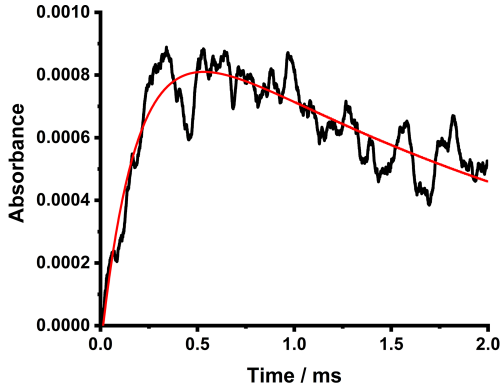

Figure 7. Time-resolved absorbance signals for SO_3 obtained at a wavenumber of $\sim 1388.7\,cm^{-1}$. Data are averages of 250 photolysis shots at a total pressure of 50 Torr at 298 K with $[SO_2] = 2.1 \times 10^{14}\,cm^{-3}$ and $[CH_2I_2] = 1.6 \times 10^{14}\,cm^{-3}$. The fit to Eq. (3) to determine the kinetics describing the production and loss of SO_3 (red) gave $k_{growth} = (8250 \pm 60)\,s^{-1}$ and $k_{loss} = (300 \pm 10)\,s^{-1}$.

Further experiments were performed with the CH_2I_2–O_2–N_2–SO_2 system to monitor the production of SO_3 at $\sim 1388.7\,cm^{-1}$. Previous work in this laboratory has demonstrated that HCHO is produced in Reaction (R5) (Stone et al., 2014), and theory has predicted the co-production of SO_3 (Vereecken et al., 2012; Kuwata et al., 2015). Experimental work using step-scan FT-IR spectroscopy with a resolution of 1–4 cm^{-1} has indicated the production of SO_3 following photolysis of CH_2I_2–O_2–N_2–SO_2 mixtures (Wang et al., 2018), but kinetics of SO_3 production have yet to be reported to confirm direct production through Reaction (R5).

The QCL operating at $\sim 1390\,cm^{-1}$ was tuned to an absorption feature in the SO_3 spectrum using a sample of gaseous SO_3–N_2 in an infrared absorption cell prepared from solid SO_3 (Sigma-Aldrich, > 99 %) in a glove box purged with N_2. For experiments to monitor the kinetics of SO_3 production following photolysis of CH_2I_2–O_2–N_2–SO_2 mixtures, a PicoScope was used to collect the signal owing to lower absorbance signals for SO_3 compared to CH_2OO for given experimental conditions. The faster sampling rate and memory (5 Gs s^{-1} and 12 bit, respectively) of the PicoScope compared to the traditional LeCroy oscilloscope (sampling rate 1 Gs s^{-1} and 8 bit memory) effectively decrease the limit of detection. Factors affecting the limit of detection and the comparison between the PicoScope and the traditional oscilloscope are discussed further in Sect. 5.

Figure 7 shows examples of the time-resolved SO_3 absorbance, which can be described by a pseudo-first-order growth combined with a first-order loss (Eq. 3) and used to

Please note the remarks at the end of the manuscript.

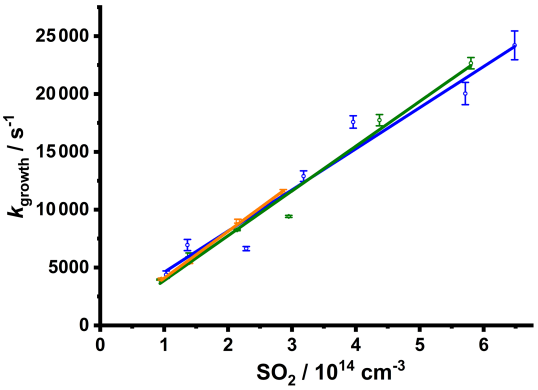

Figure 8. Bimolecular plots of the pseudo-first-order rate coefficients, k' TS4, determined from the observed SO_3 profiles as a function of $[SO_2]$. Data were obtained at total pressures of 20 Torr (blue points and line; giving $k_5 = (3.55 \pm 0.35) \times 10^{-11}$ cm^3 s^{-1}, intercept $= (1000 \pm 1400\,\mathrm{s}^{-1})$), 50 Torr (green points and line; giving $k_5 = (3.87 \pm 0.28) \times 10^{-11}$ cm^3 s^{-1}, intercept $= (100 \pm 900$ s$^{-1})$), and 100 Torr (orange points and line; giving $k_5 = (4.05 \pm 0.19) \times 10^{-11}$ cm^3 s^{-1}, intercept $= (400 \pm 400\,\mathrm{s}^{-1})$). The data compare well to the current IUPAC recommendation of $\left(3.70^{+0.45}_{-0.40}\right) \times 10^{-11}$ cm^3 s^{-1} (Cox et al., 2020). Error bars are 1σ from the fits to Eq. (3).

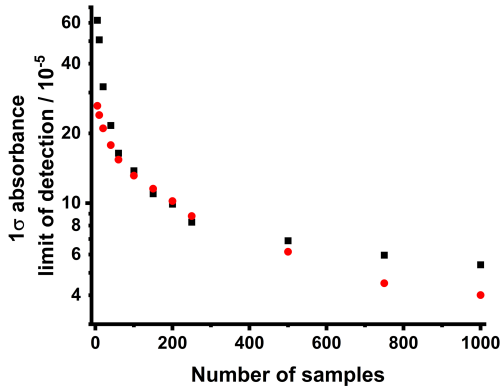

Figure 9. Variation in the 1σ limit of detection with the number of samples, which is equivalent to the number of photolysis shots for measurements involving reactive species. The 1σ limit of detection is defined as the standard deviation of the baseline absorbance and is given for the time period equivalent to the pre-photolysis period (-4000 to -500 µs, where $t = 0$ is the time at which the photolysis laser is fired) for measurements of reactive species. Measurements are shown for the traditional oscilloscope (LeCroy WaveRunner-2, LT262, 350 MHz, 1 GS s^{-1} sample rate, 8 bit resolution) in black and the PicoScope (Pico Technology, PicoScope 6402C, 250 MHz, 5 GS s^{-1} sample rate, 12 bit resolution) in red.

provide an alternative determination of k_5.

$$A_t = \frac{A_0 k_{\mathrm{growth}}}{\left(k_{\mathrm{growth}} - k_{\mathrm{loss}}\right)} \left\{ e^{-k_{\mathrm{loss}} t} - e^{-k_{\mathrm{growth}} t} \right\}, \tag{3}$$

where A_t is the absorbance at time t; A_0 refers to the maximum absorbance, which relates to the initial radical concentration and yield of SO_3; k_{growth} is the pseudo-first-order rate coefficient describing the growth of SO_3, which is equal to $k_5[SO_2]$; and k_{loss} is the first-order rate coefficient describing the loss of SO_3, which is expected to be dominated by physical losses such as diffusion out of the probe region.

The bimolecular plots obtained through SO_3 measurements at total pressures of 20, 50, and 100 Torr are shown in Fig. 8 and demonstrate the capability of the instrument to measure the kinetics describing product formation to at least 25 000 s^{-1}. The bimolecular plots give $k_5 = (3.55 \pm 0.35) \times 10^{-11}$ cm^3 s^{-1} at 20 Torr, $(3.87 \pm 0.28) \times 10^{-11}$ cm^3 s^{-1} at 50 Torr, and $(4.05 \pm 0.19) \times 10^{-11}$ cm^3 s^{-1} at 100 Torr, in excellent agreement with that determined through measurements of CH_2OO described above and the current IUPAC recommendation (Cox et al., 2020). These results thus demonstrate direct production of SO_3 through Reaction (R5) and the capability of the experiment to identify and monitor reaction products.

5 Limit of detection

The limit of detection can be determined from the variability in the baseline absorbance (i.e. in the absence of any absorbing species), which should be equal to zero and for which deviations from zero are determined only by noise. In order to detect an absorbance signal above the baseline, the signal must be greater than the noise (i.e. the signal-to-noise ratio must be greater than 1), and the limit of detection can thus be defined as the standard deviation of the noise. Figure 9 shows how the 1σ limit of detection varies with the number of samples, which for measurements involving reactive species (Sect. 4) is equal to the number of photolysis shots and is determined for the baseline given for the pre-photolysis period (-4000 to -500 µs, where $t = 0$ is the time at which the photolysis laser is fired).

The limit of detection is given for measurements with the traditional oscilloscope and the PicoScope, with some improvement to the limit of detection achieved when using the PicoScope, owing to greater memory and sampling rate (12 bit and 5 Gs s^{-1}) compared to the traditional oscilloscope (8 bit and 1 G s^{-1}), which effectively increases the number of measurement points within a sample within a given time period. For the traditional oscilloscope, a limit of detection of 8.3×10^{-5}, in absorbance terms, is achieved for 250 samples, which is reduced to 5.4×10^{-5} for 1000 samples. For the estimated path length of (218 ± 20) cm and typical IR absorption cross-sections of $\sim 10^{-19}$ cm^2, the limit of detection for these data in terms of concentration can thus be estimated as $\sim 3.8 \times 10^{12}$ cm^{-3} for 250 samples and $\sim$

Please note the remarks at the end of the manuscript.

2.5×10^{12} cm^{-3} for 1000 samples, which compares well with alternative IR-based techniques (Taatjes and Hershberger, 2001; Roberts et al., 2020). For measurements of CH_2OO, which has relatively high-IR-absorption cross-sections on the order of 10^{-18} cm^2 at ~ 1286 cm^{-1}, the limit of detection for 250 samples using the traditional oscilloscope is thus $\sim 2.5 \times 10^{11}$ cm^{-3}. For the PicoScope, the limit of detection is significantly better than that for the traditional oscilloscope when the number of samples is low, with the limits of detection becoming more comparable as the number of samples is increased. For 1000 measurements, the PicoScope gives a limit of detection of 4.0×10^{-5} in absorbance terms, which for species with IR cross-sections on the order of $\sim 10^{-19}$ cm^2 gives a limit of detection of $\sim 1.8 \times 10^{12}$ cm^{-3} in terms of concentration. For CH_2OO, with relatively high IR cross-sections of $\sim 10^{-18}$ cm^2 at ~ 1286 cm^{-1}, the limit of detection is thus on the order of $\sim 1.8 \times 10^{11}$ cm^{-3}.

6 Conclusions and future improvements

This work presents the characterisation and initial experiments performed using a new instrument based on mid-infrared QCL absorption spectroscopy to investigate the chemistry of reactive species with high spectral and temporal resolution. We present details of the experimental set-up (Sect. 2), results obtained for time-averaged measurements of stable species (Sect. 3), and results for time-resolved measurements of reactive species (Sect. 4).

We have demonstrated the application of the instrument to measurements of the IR spectra of reactive species which can be used to identify reactive species and their reaction products as well as to monitor reaction kinetics. The capabilities of the instrument have been demonstrated through measurements of the ν_4 band of the infrared spectrum of the CH_2OO Criegee intermediate, produced by laser flash photolysis of CH_2I_2–O_2–N_2 gas mixtures at $\lambda = 266$ nm, and through measurements of the kinetics of the reaction between CH_2OO and SO_2 under a range of conditions. The results have demonstrated the ability to measure reaction kinetics through monitoring of either reactants or reaction products, with the potential for the identification of reaction products and measurements of product yields. Results have shown that SO_3 is a reaction product in the reaction of CH_2OO with SO_2, with preliminary results indicating that there is no pressure dependence in the yield of SO_3.

The instrument described in this work has applications in atmospheric chemistry and chemical kinetics, with wider potential uses in trace gas analysis in industrial processes and medical diagnostics. Future development of the instrument will focus on improvements in the signal-to-noise ratio and limit of detection. Improvements to the limit of detection could be achieved through further increases to the sampling rate and through the use of a balanced detector or lock-in amplification techniques to improve the signal-to-noise ratio. Additional improvements to the limit of detection in concentration terms are achievable through the use of a mirror arrangement for the probe beam in which the optics are internal to the reaction cell, thereby reducing intensity losses as the probe beam passes through the cell windows on each pass through the cell and enabling significant increases to the effective path length.

Code availability. Code can be provided on request.

Data availability. Data can be provided on request.

Author contributions. ZSM, MJ, and DS performed the experiments and analysed the data, with support from MAB and PWS. NRG developed the custom LabVIEW software to operate the instrument. DS wrote the manuscript. All authors provided comments on the analysis and the manuscript.

Competing interests. The contact author has declared that neither they nor their co-authors have any competing interests.

Disclaimer. Publisher's note: Copernicus Publications remains neutral with regard to jurisdictional claims in published maps and institutional affiliations.

Acknowledgements. The authors would like to thank the Natural Environment Research Council (NERC) for funding (grant references NE/L010798/1 and NE/P012876/1) and for the award of a studentship as part of the SPHERES DTP scheme.

Financial support. This research has been supported by the Natural Environment Research Council (grant nos. NE/L010798/1 and NE/P012876/1).

Review statement. This paper was edited by Hartwig Harder and reviewed by two anonymous referees.

References

Atkinson, R., Baulch, D. L., Cox, R. A., Crowley, J. N., Hampson, R. F., Hynes, R. G., Jenkin, M. E., Rossi, M. J., Troe, J., and Wallington, T. J.: Evaluated kinetic and photochemical data for atmospheric chemistry: Volume IV – gas phase reactions of organic halogen species, Atmos. Chem. Phys., 8, 4141–4496, https://doi.org/10.5194/acp-8-4141-2008, 2008.

Banik, G. D., Som, S., Maity, A., Pal, M., Maithani, S., Mandal, S., and Pradhan, M.: An EC-QCL based N_2O sensor at 5.2 µm using cavity ring-down spectroscopy for environmental applications,

Anal. Meth., 9, 2315–2320, https://doi.org/10.1039/c7ay00482f, 2017.

Bjork, B. J., Bui, T. Q., Heckl, O. H., Changala, P. B., Spaun, B., Heu, P., Follman, D., Deutsch, C., Cole, G. D., Aspelmeyer, M., Okumura, M., and Ye, J.: Direct frequency comb measurement of OD plus CO − > DOCO kinetics, Science, 354, 444–448, https://doi.org/10.1126/science.aag1862, 2016.

Blitz, M. A. and Seakins, P. W.: Laboratory studies of photochemistry and gas phase radical reaction kinetics relevant to planetary atmospheres, Chem. Soc. Rev., 41, 6318–6347, https://doi.org/10.1039/c2cs35204d, 2012.

Blitz, M. A., Goddard, A., Ingham, T., and Pilling, M. J.: Time-of-flight mass spectrometry for time-resolved measurements, Rev. Sci. Instr., 78, 1–9, https://doi.org/10.1063/1.2712797, 2007.

Borri, S., Bartalini, S., De Natale, P., Inguscio, M., Gmachl, C., Capasso, F., Sivco, D. L., and Cho, A. Y.: Frequency modulation spectroscopy by means of quantum-cascade lasers, Appl. Phys. B., 85, 223–229, https://doi.org/10.1007/s00340-006-2343-6, 2006.

Carr, S. A., Baeza-Romero, M. T., Blitz, M. A., Pilling, M. J., Heard, D. E., and Seakins, P. W.: OH yields from the CH_3CO+O_2 reaction using an internal standard, Chem. Phys. Lett., 445, 108–112, https://doi.org/10.1016/j.cplett.2007.07.099, 2007.

Chang, Y. P., Chang, H. H., and Lin, J. J. M.: Kinetics of the simplest Criegee intermediate reaction with ozone studied using a mid-infrared quantum cascade laser spectrometer, Phys. Chem. Chem. Phys., 20, 97–102, https://doi.org/10.1039/c7cp06653h, 2018a.

Chang, Y. P., Li, Y. L., Liu, M. L., Ou, T. C., and Lin, J. J. M.: Absolute Infrared Absorption Cross Section of the Simplest Criegee Intermediate Near 1285.7 cm^{-1}, J. Phys. Chem. A, 122, 8874–8881, https://doi.org/10.1021/acs.jpca.8b06759, 2018b.

Chang, Y. P., Merer, A. J., Chang, H. H., Jhang, L. J., Chao, W., and Lin, J. J. M.: High resolution quantum cascade laser spectroscopy of the simplest Criegee intermediate, CH_2OO, between 1273 cm^{-1} and 1290 cm^{-1}, J. Chem. Phys., 146, 1–9, https://doi.org/10.1063/1.4986536, 2017.

Chattopadhyay, A., Samanta, M., Mondal, K., and Chakraborty, T.: Mid-infrared quantum cascade laser spectroscopy probing of the kinetics of an atmospherically significant radical reaction, $CH_3O_2+ NO_2+ M$ ->$CH_3O_2NO_2+ M$, in the gas phase, J. Chem. Sci., 130, 1–10, https://doi.org/10.1007/s12039-018-1451-2, 2018.

Chhantyal-Pun, R., Khan, M. A. H., Taatjes, C. A., Percival, C. J., Orr-Ewing, A. J., and Shallcross, D. E.: Criegee intermediates: production, detection and reactivity, Int. Rev. Phys. Chem., 39, 383–422, https://doi.org/10.1080/0144235x.2020.1792104, 2020.

Choi, N., Pilling, M. J., Seakins, P. W., and Wang, L.: Studies of site selective hydrogen atom abstractions by Cl atoms from isobutane and propane by laser flash photolysis/IR diode laser spectroscopy, Phys. Chem. Chem. Phys., 8, 2172–2178, https://doi.org/10.1039/b516531h, 2006.

Cossel, K. C., Waxman, E. M., Finneran, I. A., Blake, G. A., Ye, J., and Newbury, N. R.: Gas-phase broadband spectroscopy using active sources: progress, status, and applications, J. Optic. Soc. Am. B, 34, 104–129, https://doi.org/10.1364/josab.34.000104, 2017.

Cox, R. A., Ammann, M., Crowley, J. N., Herrmann, H., Jenkin, M. E., McNeill, V. F., Mellouki, A., Troe, J., and Wallington, T. J.: Evaluated kinetic and photochemical data for atmospheric chemistry: Volume VII – Criegee intermediates, Atmos. Chem. Phys., 20, 13497–13519, https://doi.org/10.5194/acp-20-13497-2020, 2020.

Cui, X. J., Yu, R. Q., Chen, W. D., Zhang, Z. R., Pang, T., Sun, P. S., Xia, H., Wu, B., and Dong, F. Z.: Development of a Quantum Cascade Laser-Based Sensor for Environmental HONO Monitoring in the Mid-Infrared at 8 µm, J. Lightwave Tech., 37, 2784–2791, https://doi.org/10.1109/jlt.2018.2876672, 2019.

Curl, R. F., Capasso, F., Gmachl, C., Kosterev, A. A., McManus, B., Lewicki, R., Pusharsky, M., Wysocki, G., and Tittel, F. K.: Quantum cascade lasers in chemical physics, Chem. Phys. Lett., 487, 1–18, https://doi.org/10.1016/j.cplett.2009.12.073, 2010.

Doussin, J. F., Ritz, D., DurandJolibois, R., Monod, A., and Carlier, P.: Design of an environmental chamber for the study of atmospheric chemistry: New developments in the analytical device, Analusis, 25, 236–242, 1997.

Du, Z. H., Zhang, S., Li, J. Y., Gao, N., and Tong, K. B.: Mid-Infrared Tunable Laser-Based Broadband Fingerprint Absorption Spectroscopy for Trace Gas Sensing: A Review, Appl. Sci., 9, 1–33, https://doi.org/10.3390/app9020338, 2019.

Eskola, A. J., Wojcik-Pastuszka, D., Ratajczak, E., and Timonen, R. S.: Kinetics of the reactions of CH_2Br and CH_2I radicals with molecular oxygen at atmospheric temperatures, Phys. Chem. Chem. Phys., 8, 1416–1424, https://doi.org/10.1039/b516291b, 2006.

FACSIMILE: MCPA Software Ltd., https://www.mcpa-software.com/ (last access: TS5), 2014.

Faist, J., Capasso, F., Sivco, D. L., Sirtori, C., Hutchinson, A. L., and Cho, A. Y.: Quantum Cascade Laser, Science, 264, 553–556, https://doi.org/10.1126/science.264.5158.553, 1994.

Fleisher, A. J., Bjork, B. J., Bui, T. Q., Cossel, K. C., Okumura, M., and Ye, J.: Mid-Infrared Time-Resolved Frequency Comb Spectroscopy of Transient Free Radicals, J. Phys. Chem. Lett., 5, 2241–2246, https://doi.org/10.1021/jz5008559, 2014.

Fockenberg, C., Bernstein, H. J., Hall, G. E., Muckerman, J. T., Preses, J. M., Sears, T. J., and Weston, R. E.: Repetitively sampled time-of-flight mass spectrometry for gas-phase kinetics studies, Rev. Sci. Instr., 70, 3259–3264, https://doi.org/10.1063/1.1149944, 1999.

Glowacki, D. R., Goddard, A., Hemavibool, K., Malkin, T. L., Commane, R., Anderson, F., Bloss, W. J., Heard, D. E., Ingham, T., Pilling, M. J., and Seakins, P. W.: Design of and initial results from a Highly Instrumented Reactor for Atmospheric Chemistry (HIRAC), Atmos. Chem. Phys., 7, 5371–5390, https://doi.org/10.5194/acp-7-5371-2007, 2007.

Gmachl, C., Capasso, F., Sivco, D. L., and Cho, A. Y.: Recent progress in quantum cascade lasers and applications, Rep. Prog. Phys., 64, 1533–1601, https://doi.org/10.1088/0034-4885/64/11/204, 2001.

Gordon, I. E., Rothman, L. S., Hill, C., Kochanov, R. V., Tan, Y., Bernath, P. F., Birk, M., Boudon, V., Campargue, A., Chance, K. V., Drouin, B. J., Flaud, J. M., Gamache, R. R., Hodges, J. T., Jacquemart, D., Perevalov, V. I., Perrin, A., Shine, K. P., Smith, M. A. H., Tennyson, J., Toon, G. C., Tran, H., Tyuterev, V. G., Barbe, A., Csaszar, A. G., Devi, V. M., Furtenbacher, T., Harrison, J. J., Hartmann, J. M., Jolly, A., Johnson, T. J., Kar-

Please note the remarks at the end of the manuscript.

man, T., Kleiner, I., Kyuberis, A. A., Loos, J., Lyulin, O. M., Massie, S. T., Mikhailenko, S. N., Moazzen-Ahmadi, N., Muller, H. S. P., Naumenko, O. V., Nikitin, A. V., Polyansky, O. L., Rey, M., Rotger, M., Sharpe, S. W., Sung, K., Starikova, E., Tashkun, S. A., Vander Auwera, J., Wagner, G., Wilzewski, J., Wcislo, P., Yu, S., and Zak, E. J.: The HITRAN2016 molecular spectroscopic database, J. Quant. Spec. Rad. Trans., 203, 3–69, https://doi.org/10.1016/j.jqsrt.2017.06.038, 2017.

Gravestock, T. J., Blitz, M. A., Bloss, W. J., and Heard, D. E.: A Multidimensional Study of the Reaction $CH_2I + O_2$: Products and Atmospheric Implications, Chem. Phys. Chem, 11, 3928–3941, https://doi.org/10.1002/cphc.201000575, 2010.

Herbst, E.: The chemistry of interstellar space, Chem. Soc. Rev., 30, 168–176, https://doi.org/10.1039/a909040a, 2001.

Herndon, S. C., Zahniser, M. S., Nelson, D. D., Shorter, J., McManus, J. B., Jimenez, R., Warneke, C., and de Gouw, J. A.: Airborne measurements of HCHO and HCOOH during the New England Air Quality Study 2004 using a pulsed quantum cascade laser spectrometer, J. Geophys. Res. Atmos., 112, 1–15, https://doi.org/10.1029/2006jd007600, 2007.

Hodgkinson, J. and Tatam, R. P.: Optical gas sensing: a review, Meas. Sci. Technol., 24, 1–59, https://doi.org/10.1088/0957-0233/24/1/012004, 2013.

Hofstetter, D. and Faist, J.: High Performance Quantum Cascade Lasers and Their Applications, in: Solid-State Mid-Infrared Laser Sources. Topics in Applied Physics, edited by: Sorokina, I. T. and Vodopyanov, K. L., Vol 89. Springer, Berlin, Heidelberg, https://doi.org/10.1007/3-540-36491-9_2, 2003.

Huang, D. R., Chu, L. K., and Lee, Y. P.: Infrared absorption of gaseous CH_3OO detected with a step-scan Fourier-transform spectrometer, J. Chem. Phys., 127, 1–7, https://doi.org/10.1063/1.2807241, 2007.

Kochanov, R. V., Gordon, I. E., Rothman, L. S., Shine, K. P., Sharpe, S. W., Johnson, T. J., Wallington, T. J., Harrison, J. J., Bernath, P. F., Birk, M., Wagner, G., Le Bris, K., Bravo, I., and Hill, C.: Infrared absorption cross-sections in HITRAN2016 and beyond: Expansion for climate, environment, and atmospheric applications, J. Quant. Spec. Rad. Trans., 230, 172–221, https://doi.org/10.1016/j.jqsrt.2019.04.001, 2019.

Kostinek, J., Roiger, A., Davis, K. J., Sweeney, C., DiGangi, J. P., Choi, Y., Baier, B., Hase, F., Groß, J., Eckl, M., Klausner, T., and Butz, A.: Adaptation and performance assessment of a quantum and interband cascade laser spectrometer for simultaneous airborne in situ observation of CH_4, C_2H_6, CO_2, CO and N_2O, Atmos. Meas. Tech., 12, 1767–1783, https://doi.org/10.5194/amt-12-1767-2019, 2019.

Kuwata, K. T., Guinn, E. J., Hermes, M. R., Fernandez, J. A., Mathison, J. M., and Huang, K.: A Computational Re-examination of the Criegee Intermediate-Sulfur Dioxide Reaction, J. Phys. Chem. A, 119, 10316–10335, https://doi.org/10.1021/acs.jpca.5b06565, 2015.

Lewis, T., Heard, D. E., and Blitz, M. A.: A novel multiplex absorption spectrometer for time-resolved studies, Rev. Sci. Instr., 89, 1–8, https://doi.org/10.1063/1.5006539, 2018.

Li, J. S., Chen, W., and Fischer, H.: Quantum Cascade Laser Spectrometry Techniques: A New Trend in Atmospheric Chemistry, Appl. Spec. Rev., 48, 523–559, https://doi.org/10.1080/05704928.2012.757232, 2013.

Li, Y. L., Lin, C. Y., Lin, Y. H., and Lin, J. J. M.: Temperature-dependent kinetics of the simplest Criegee intermediate reaction with dimethyl sulfoxide, J. Chin. Chem. Soc., 67, 1563–1570, https://doi.org/10.1002/jccs.202000206, 2020.

Li, Y. L., Lin, Y. H., Yin, C. T., Takahashi, K., Chiang, C. Y., Chang, Y. P., and Lin, J. J. M.: Temperature-Dependent Rate Coefficient for the Reaction of CH_3SH with the Simplest Criegee Intermediate, J. Phys. Chem. A, 123, 4096–4103, https://doi.org/10.1021/acs.jpca.8b12553, 2019.

Luo, P. L., Chung, C. A., and Lee, Y. P.: Rate coefficient of the reaction $CH_2OO + NO_2$ probed with a quantum-cascade laser near 11 µm, Phys. Chem. Chem. Phys., 21, 17578–17583, https://doi.org/10.1039/c9cp03333e, 2019.

Luo, P. L., Endo, Y., and Lee, Y. P.: High-resolution vibration-rotational spectra and rotational perturbation of the OO-stretching ($\nu(6)$) band of CH_2OO between 879.5 and 932.0 cm^{-1}, Phys. Chem. Chem. Phys., 20, 25806–25811, https://doi.org/10.1039/c8cp04780d, 2018a.

Luo, P. L., Endo, Y., and Lee, Y. P.: Identification and Self-Reaction Kinetics of Criegee Intermediates *syn*-CH_3CHOO and CH_2OO via High-Resolution Infrared Spectra with a Quantum-Cascade Laser, J. Phys. Chem. Lett., 9, 4391–4395, https://doi.org/10.1021/acs.jpclett.8b01824, 2018b.

Masaki, A., Tsunashima, S., and Washida, N.: Rate constants for reactions of substituted methyl radicals (CH_2OCH_3, CH_2NH_2, CH_2I, and CH_2CN) with O_2, J. Phys. Chem., 99, 13126–13131, https://doi.org/10.1021/j100035a014, 1995.

McManus, J. B., Zahniser, M. S., Nelson, D. D., Shorter, J. H., Herndon, S., Wood, E., and Wehr, R.: Application of quantum cascade lasers to high-precision atmospheric trace gas measurements, Opt. Eng., 49, 1–11, https://doi.org/10.1117/1.3498782, 2010.

Middaugh, J. E., Buras, Z. J., Matrat, M., Chu, T. C., Kim, Y. S., Alecu, I. M., Vasiliou, A. K., Goldsmith, C. F., and Green, W. H.: A combined photoionization time-of-flight mass spectrometry and laser absorption spectrometry flash photolysis apparatus for simultaneous determination of reaction rates and product branching, Rev. Sci. Instr., 89, 1–19, https://doi.org/10.1063/1.5024399, 2018.

Mir, Z. S., Lewis, T. R., Onel, L., Blitz, M. A., Seakins, P. W., and Stone, D.: CH_2OO Criegee intermediate UV absorption cross-sections and kinetics of $CH_2OO + CH_2OO$ and $CH_2OO + I$ as a function of pressure, Phys. Chem. Chem. Phys., 22, 9448–9459, https://doi.org/10.1039/d0cp00988a, 2020.

Miyano, S. and Tonokura, K.: Measurements of nitrogen-broadening coefficients in the nu(3) band of the hydroperoxyl radical using a continuous wave quantum cascade laser, J. Mol. Spec., 265, 47–51, https://doi.org/10.1016/j.jms.2010.10.010, 2011.

Monks, P. S.: Gas-phase radical chemistry in the troposphere, Chem. Soc. Rev., 34, 376–395, doiL:10.1039/b307982c, 2005.

Nasir, E. F. and Farooq, A.: Cavity-enhanced absorption sensor for carbon monoxide in a rapid compression machine, Proc. Combust. Inst., 37, 1297–1304, https://doi.org/10.1016/j.proci.2018.05.015, 2019.

Nilsson, E. J. K., Eskebjerg, C., and Johnson, M. S.: A photochemical reactor for studies of atmospheric chemistry, Atmos. Environ., 43, 3029–3033, https://doi.org/10.1016/j.atmosenv.2009.02.034, 2009.

Orlando, J. J. and Tyndall, G. S.: Laboratory studies of organic peroxy radical chemistry: an overview with emphasis on recent issues of atmospheric significance, Chem. Soc. Rev., 41, 6294–6317, diu:10.1039/c2cs35166h, 2012.

Osborn, D. L., Zou, P., Johnsen, H., Hayden, C. C., Taatjes, C. A., Knyazev, V. D., North, S. W., Peterka, D. S., Ahmed, M., and Leone, S. R.: The multiplexed chemical kinetic photoionization mass spectrometer: A new approach to isomer-resolved chemical kinetics, Rev. Sci. Instr., 79, 1–10, https://doi.org/10.1063/1.3000004, 2008.

Pecharroman-Gallego, R.: Quantum Cascade Lasers: Review, Applications and Prospective Development, Lasers Engin., 24, 277–314, 2013.

Percival, C. J., Welz, O., Eskola, A. J., Savee, J. D., Osborn, D. L., Topping, D. O., Lowe, D., Utembe, S. R., Bacak, A., McFiggans, G., Cooke, M. C., Xiao, P., Archibald, A. T., Jenkin, M. E., Derwent, R. G., Riipinen, I., Mok, D. W. K., Lee, E. P. F., Dyke, J. M., Taatjes, C. A., and Shallcross, D. E.: Regional and global impacts of Criegee intermediates on atmospheric sulphuric acid concentrations and first steps of aerosol formation, Farad. Discuss., 165, 45–73, 10.1039/c3fd00048f, 2013.

Pilling, M. J., Robertson, S. H., and Seakins, P. W.: Elementary radical reactions and autoignition, J. Chem. Soc. Farad. Trans., 91, 4179–4188, https://doi.org/10.1039/ft9959104179, 1995.

Qian, H. B., Turton, D., Seakins, P. W., and Pilling, M. J.: Dynamic frequency stabilization of infrared diode laser for kinetic studies, Chem. Phys. Lett., 322, 57–64, https://doi.org/10.1016/s0009-2614(00)00395-x, 2000.

Qian, H. B., Turton, D., Seakins, P. W., and Pilling, M. J.: A laser flash photolysis/IR diode laser absorption study of the reaction of chlorine atoms with selected alkanes, Int. J. Chem. Kinet., 34, 86–94, 2001.

Roberts, F. C., Lewandowski, H. J., Hobson, B. F., and Lehman, J. H.: A rapid, spatially dispersive frequency comb spectrograph aimed at gas phase chemical reaction kinetics, Mol. Phys., 118, 1–9, https://doi.org/10.1080/00268976.2020.1733116, 2020.

Sakamoto, Y. and Tonokura, K.: Measurements of the Absorption Line Strength of Hydroperoxyl Radical in the nu(3) Band using a Continuous Wave Quantum Cascade Laser, J. Phys. Chem. A, 116, 215–222, https://doi.org/10.1021/jp207477n, 2012.

Seakins, P. W.: Product branching ratios in simple gas phase reactions, Ann. Rep. Sect. C Phys. Chem., 103, 173–222, https://doi.org/10.1039/B605650B, 2007.

Seakins, P. W.: A brief review of the use of environmental chambers for gas phase studies of kinetics, chemical mechanisms and characterisation of field instruments, in: Erca 9: From the Global Mercury Cycle to the Discoveries of Kuiper Belt Objects, edited by: Boutron, C., EPJ Web of Conferences, 143–163, https://doi.org/10.1051/epjconf/201009012, 2010.

Shahmohammadi, M., Kapsalidis, F., Suess, M. J., Gini, E., Beck, M., Hundt, M., Tuzson, B., Emmenegger, L., and Faist, J.: Multi-wavelength distributed feedback quantum cascade lasers for broadband trace gas spectroscopy, Semicond. Sci. Technol., 34, 1–14, https://doi.org/10.1088/1361-6641/ab2838, 2019.

Stone, D., Blitz, M., Daubney, L., Howes, N. U. M., and Seakins, P.: Kinetics of CH_2OO reactions with SO_2, NO_2, NO, H_2O and CH_3CHO as a function of pressure, Phys. Chem. Chem. Phys., 16, 1139–1149, https://doi.org/10.1039/c3cp54391a, 2014.

Stone, D., Blitz, M., Daubney, L., Ingham, T., and Seakins, P.: CH_2OO Criegee biradical yields following photolysis of CH_2I_2 in O_2, Phys. Chem. Chem. Phys., 15, 19119–19124, https://doi.org/10.1039/c3cp52466c, 2013.

Su, Y. T., Huang, Y. H., Witek, H. A., and Lee, Y. P.: Infrared Absorption Spectrum of the Simplest Criegee Intermediate CH_2OO, Science, 340, 174–176, https://doi.org/10.1126/science.1234369, 2013.

Taatjes, C. A. and Hershberger, J. F.: Recent progress in infrared absorption techniques for elementary gas-phase reaction kinetics, Ann. Rev. Phys. Chem., 52, 41–70, https://doi.org/10.1146/annurev.physchem.52.1.41, 2001.

Vereecken, L., Harder, H., and Novelli, A.: The reaction of Criegee intermediates with NO, RO_2, and SO_2, and their fate in the atmosphere, Phys. Chem. Chem. Phys., 14, 14682–14695, https://doi.org/10.1039/c2cp42300f, 2012.

von Schneidemesser, E., Monks, P. S., Allan, J. D., Bruhwiler, L., Forster, P., Fowler, D., Lauer, A., Morgan, W. T., Paasonen, P., Righi, M., Sindelarova, K., and Sutton, M. A.: Chemistry and the Linkages between Air Quality and Climate Change, Chem. Rev., 115, 3856–3897, https://doi.org/10.1021/acs.chemrev.5b00089, 2015.

Wang, Y. Y., Dash, M. R., Chung, C. Y., and Lee, Y. P.: Detection of transient infrared absorption of SO_3 and 1,3,2-dioxathietane-2,2-dioxide cyc-$(CH_2)O(SO_2)O$ in the reaction CH_2OO+SO_2, J. Chem. Phys., 148, 1–9, https://doi.org/10.1063/1.5019205, 2018.

Welz, O., Savee, J. D., Osborn, D. L., Vasu, S. S., Percival, C. J., Shallcross, D. E., and Taatjes, C. A.: Direct Kinetic Measurements of Criegee Intermediate (CH_2OO) Formed by Reaction of CH_2I with O_2, Science, 335, 204–207, https://doi.org/10.1126/science.1213229, 2012.

Yao, Y., Hoffman, A. J., and Gmachl, C. F.: Mid-infrared quantum cascade lasers, Nature Photonics, 6, 432–439, https://doi.org/10.1038/nphoton.2012.143, 2012.

Zador, J., Taatjes, C. A., and Fernandes, R. X.: Kinetics of elementary reactions in low-temperature autoignition chemistry, Prog. Ener. Combust. Sci., 37, 371–421, https://doi.org/10.1016/j.pecs.2010.06.006, 2011.

Zhang, L. Z., Tian, G., Li, J. S., and Yu, B. L.: Applications of Absorption Spectroscopy Using Quantum Cascade Lasers, Appl. Spec., 68, 1095–1107, https://doi.org/10.1366/14-00001, 2014.

Remarks from the language copy-editor

CE1 If you feel the meaning has been changed through the hyphenation, please let me know what the intended meaning is. However, if you mean “cross-sections of low UV absorption” (i.e., “low UV absorption” acts as an adjective to “cross-sections”), the hyphenation is necessary here as it would be in any other phrase with a similar construction.

Remarks from the typesetter

TS1 **Dear Editor: add “M” over the arrow leading to CH_2IO_2.**
TS2 **Dear Editor: add “M” over the arrow leading to CH_2IO_2.**
TS3 **Dear Editor: removing "=0".**
TS4 **Dear Editor: Change k' to k_{growth}.**
TS5 For every link mentioned in the paper we need a last access date. This ensures that the link was working, when you visited it the last time. Please, provide your last access date.